Inorganic Chemistry

pubs.acs.org/IC Article

# Probing the Origins of Puzzling Reactivity in Fe/Mn−Oxo/Hydroxo Species toward C−H Bonds: A DFT and Ab Initio Perspective

Asmita Sen, Azaj Ansari, Abinash Swain, Bhawana Pandey, and Gopalan Rajaraman*

Cite This: *Inorg. Chem.* 2023, 62, 14931−14941 Read Online

ACCESS | Metrics & More | Article Recommendations | Supporting Information

**ABSTRACT:** Activation of C−H bonds using an earth-abundant metal catalyst is one of the top challenges of chemistry, where high-valent Mn/Fe−oxo(hydroxo) biomimic species play an important role. There are several open questions related to the comparative oxidative abilities of these species, and a unifying concept that could accommodate various factors influencing reactivity is lacking. To shed light on these open questions, here, we have used a combination of density functional theory (DFT) (B3LYP-D3/def2-TZVP) and *ab initio* (CASSCF/NEVPT2) calculations to study a series of high-valent metal−oxo species $[M^{n+}H_3buea(O/OH)]$ (M = Mn and Fe, *n* = II to V; $H_3buea$ = tris[(*N*′-*tert*-butylureaylato)-*N*-ethylene)]-aminato towards the activation of dihydroanthracene (DHA). The H-bonding network in the ligand architecture influences the ground state−excited state gap and brings several excited states of the same spin multiplicity closer in energy, which triggers reactivity via one of those excited states, reducing the kinetic barriers for the C−H bond activation and rationalizing several puzzling reactivity trends observed in various high-valent Mn/Fe−oxo(hydroxo) species.

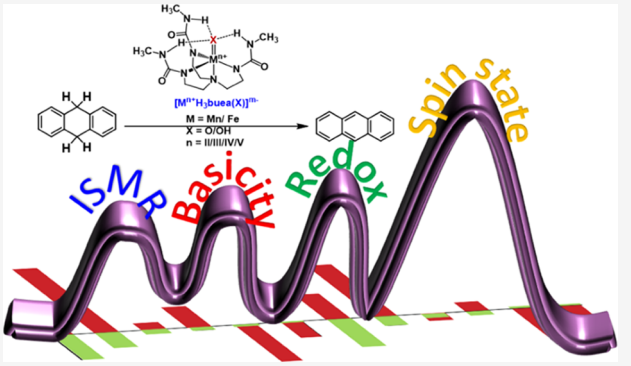


## INTRODUCTION

Aliphatic C−H bond activation is challenging in synthetic chemistry due to its very high thermodynamic stability.[1] Studies over the past few decades have proven that the nonheme high-valent manganese and iron complexes with terminal oxo ligands are potential in various oxidative transformations, including C−H bond functionalization and oxygen-atom transfer reactions, having resemblance with the active site of many biological systems, such as peroxidases, halogenases,[2,3] and in the oxygen-evolving complex (OEC) of photosystem II.[4]

In the past few decades, several experimental groups have been working extensively in this area to structurally and functionally mimic the reactivity of naturally occurring metalloenzymes. In this direction, the first prototypical $Fe^{IV}$=O intermediate, TauD-*J* (taurine: $\alpha$-ketoglutarate dioxygenase having five-coordinate trigonal bipyramidal (TBP) geometry), has been trapped and spectroscopically characterized to possess a high-spin ($S$ = 2) ground state,[5] followed by the synthesis and characterization of numerous nonheme $Fe^{IV}$=O complexes to comprehend their role in biomimic chemistry.[6−9] These terminal nonheme $Fe^{IV}$=O species are found to be the most powerful and extensively studied oxidants targeting aliphatic C−H bonds. On the other hand, the one-electron reduced $Fe^{III}$=O and one-electron oxidized $Fe^{V}$=O derivatives are comparatively rare and less explored. While a handful of biomimic complexes of $Fe^{V}$=O have been reported and characterized,[10−12] only two terminal $Fe^{III}$=O complexes are reported to date, and both of them are known to stabilize in the presence of secondary coordination sphere.[13−15] Besides the Fe−oxo complexes, the Mn−oxo model complexes also stimulate inorganic chemists owing to their possible roles in water oxidation carried out by photosystem II. In Mn chemistry, $Mn^{III/IV/V}$=O species are relevant,[16−23] and several high-valent $Mn^{IV/V}$=O complexes have been synthesized, characterized, and found to possess aggressive oxidizing abilities, sometimes even higher than the popular $Fe^{IV}$=O species.[24,25] Though there are some isolated reports, very little is known about the oxidizing abilities of the protonated metal−oxo species of this type.

One of the most crucial factors that influence the reactivity of these species is the participation of several spin states during reactivity. Most biomimic $Fe^{IV}$=O models react via the two-state reactivity,[26] where a high-spin $S$ = 2 state is found to be the rate-determining, although the ground state is an $S$ = 1 intermediate spin state.[27,28] The concept of two-state reactivity (TSR) was attributed to the very high reactivity of $Fe^{IV}$=O species. Confusion arises as a vast majority of the $Fe^{IV}$=O

**Received:** May 18, 2023
**Published:** August 31, 2023

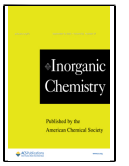

Downloaded via INDIAN INST OF TECH BOMBAY on January 6, 2024 at 08:15:19 (UTC).
See https://pubs.acs.org/sharingguidelines for options on how to legitimately share published articles.


© 2023 American Chemical Society

https://doi.org/10.1021/acs.inorgchem.3c01632
*Inorg. Chem.* 2023, 62, 14931−14941

intermediates found in metalloenzymes possess a high-spin ($S$ = 2) ground state and react without any spin crossover.[29,30] Moreover, a large body of literature collected over the years suggests that the high-spin $Fe^{IV}$=O dependent metalloenzymes react faster than those with intermediate/low-spin states without any spin crossover.[31,32] Further, some of the Mn−oxo species are found to be more reactive than their Fe analogues, and they possess a high-spin ground state, and other spin states (intermediate and low-spin) were found not to participate in the reactivity.[26,33] This puzzling reactivity demands a study across various oxo/hydroxo species of Mn and Fe to underpin the source of the variation observed.

In this direction, we have studied a series of well-characterized, $Mn/Fe^{n+}$−oxo(hydroxo) ($H_3$buea = tris[($N'$-*tert*-butylureaylato)-*N*-ethylene)]aminato ($n$ = +II to +V) complexes.[34−38] These species are structural analogues[23] and offer a unique set of structures to probe the relative oxidative abilities of these species. In this series, the experimentally observed reactivity trend contradicts the regular trend noticed in other biomimic models. For example, among the complexes studied, $[Mn^{III}H_3buea(O)]^{2-}$ was found to be the most reactive, followed by $[Fe^{III}H_3buea(O)]^{2-}$ and $[Mn^{IV}H_3buea(O)]^{-}$, while the popular $[Fe^{IV}H_3buea(O)]^{-}$ is very sluggish even with substrates, such as 1,9-dihydroanthracene (DHA), despite a fact that this substrate has the C−H bonds, which are already weak and are activated. The present study investigates the C−H bond activation by twelve different species using a combination of density functional theory (DFT) and ab initio CASSCF calculations and proposes the role of the excited state of the same spin multiplicity as the ground state in dictating the reactivity.

## COMPUTATIONAL DETAILS

**Density Functional Theory (DFT) Calculations.** All geometry optimizations were carried out with the density functional theory (DFT) method using the Gaussian 09 suite of programs.[39] The geometries of all stationary points involved in the reaction mechanism were optimized in the gas phase without any constraints using dispersion-corrected unrestricted B3LYP hybrid density functional.[40] The functional in the present study has been chosen based on our previous works[41,42] and the literature on similar Mn/Fe−oxo/hydroxo complexes (see Computational Method section in the Supporting Information). A LACVP basis set has been employed, comprising the 6-31G* description for all light atoms (H, C, N, O), and a double-$\xi$ quality LanL2DZ basis set with the Los Alamos effective core potential has been incorporated for the Mn and Fe center. The harmonic vibrational frequency and intrinsic reaction coordinate (IRC) calculations were performed to characterize the nature of the species.[43] Gas-phase electronic energies are refined by the single-point energy calculations on the optimized geometries using a def2-TZVP basis set[44] for all of the atoms in the same level of theory using Grimme's D3 version of dispersion.[45] The solvation energies have been incorporated using the solvation model based on density (SMD) solvation model[45] and def2-TZVP basis set for all. As in experiments,[35,37,46,47] *N*,*N*-dimethylacetamide (DMA) was used as a solvent in our calculations. The B3LYP-D3-computed solvation energies, incorporating the free-energy corrections obtained from the vibrational frequency calculations, have been used to estimate the potential energy surface. The spin-contamination, if found, on the broken-symmetry state, the energies were corrected using Yamaguchi's spin-projected correction formula.[48]

**Ab Initio Calculations.** When the ground-state wavefunction is admixed with the excited-state configurations, the DFT calculations being a single determinant method may not be suitable to describe a system that has a multireference character.[49] To describe these systems properly, post-Hartree−Fock multireference calculations, such as state-averaged complete active space self-consistent field (SA-CASSCF) theory, along with the incorporation of *N*-Electron Valence State Perturbation Theory (NEVPT2) to treat the dynamic correlation will be helpful.[50−53] This method is found to be appropriate for the characterization of ground spin state in open-shell cobalt complexes with redox-active ligands.[54,55] Therefore, in order to explore the involvement of multireference contributions to the ground-state wavefunction, we have used the CASSCF/NEVPT2 method in the present study. All CASSCF/NEVPT2 calculations were performed on the DFT-optimized ground-state geometries of the Mn/Fe=O complexes using the ORCA 4.2.1 program.[56,57] Scaler relativistic Hamiltonian has considered using the zeroth-order regular approximation (ZORA) method.[58] The RIJCOSX approximation with a def2/J auxiliary basis set has been employed. The starting guess orbitals were obtained by the DFT method performed using ROKS/BP86 terminology with ZORA-def2-TZVP for metal and ZORA-def2-TZVP(-f) for N, O, and ZORA-def2-SVP basis sets for the rest of the atoms (C and H). For CASSCF/NEVPT2 calculations, the active space of CAS($n$,5) and CAS($n$,8), including the five metal 3d-orbitals and their electrons and five metal 3d-orbitals along with the two oxo $p_\pi$ orbitals ($\pi_x$ and $\pi_y$) and one oxo $p_\sigma$ orbital ($\sigma_z$), are considered. For the $d^2$ metal center, 10 triplet and 15 singlet roots; for $d^3$, 10 quartet and 40 doublet roots; for the $d^4$ system, 5 quintet, 45 triplet, and 50 singlet roots; and for $d^5$, 1 sextet, 24 quartet, and 75 doublet roots are considered. In the present study, the electronic wavefunction is expanded in all possible configuration state functions distributing the electrons in the active space using the complete active space self-consistent-field (CASSCF) method. Although this method is computationally expensive, it yields reliable results when the ground-state and excited-state wavefunctions are heavily admixed. The electronic configuration of the metal complexes and the ab initio ligand field theory (AILFT) orbitals were determined by the CASSCF/NEVPT2 method using the same methodology described above. Intrinsic bond orbitals are obtained using the ORCA program, employing the unrestricted B3LYP functional coupled with the ZORA-def2-TZVP basis set for all atoms. The orbitals were calculated with the orbital localization routines in the IBOView program with a default isosurface threshold and resolution with an exponent value of 2, as recommended.[59,60]

In this manuscript, we have used the following denotation, $^{2S+1}M_{\sigma\text{-}Mn^{III}=O}$, where superscript $2S+1$ describes the multiplicity of the species, M is the name of the species; subscript $\sigma/\pi/\delta$ describes their respective orbital, which is vacant based on the CASSCF configuration. The last subscript denotes the nature of the species.

## RESULTS

**Spin-State Energetics of $M^{n+}$−O(OH) (M = Mn/Fe, $n$ = II to V) Species.** To understand in detail the relative oxidative abilities of various $M^{n+}$=O(OH) (M = Mn/Fe, $n$ = II to V)


https://doi.org/10.1021/acs.inorgchem.3c01632
Inorg. Chem. 2023, 62, 14931−14941

**Table 1. Table Containing the Ground State of All Species with CASSCF Computed Electronic Configurations, Reaction Types Involved in Various Species during the C−H Bond Activation Transition State**

| catalyst | spin state (GS) | % of mixing from CASSCF | species | reaction type |
|---|---|---|---|---|
| $Mn^{III}$−O | $S = 2$ | $\pi^*_{xz}{}^1\pi^*_{yz}{}^1\delta^*_{xy}{}^1\delta^*_{x^2-y^2}{}^1$(49%) + $\pi^*_{xz}{}^1\delta^*_{xy}{}^1\delta^*_{x^2-y^2}{}^1\sigma_{z^2}{}^1$(48%) | $^5TS_{\pi\text{-}Mn^{III}=O}$ | PT-ET |
| | | | $^5TS_{\sigma\text{-}Mn^{III}=O}$ | PCET |
| $Mn^{IV}$=O | $S = 3/2$ | $\pi^*_{yz}{}^1\delta^*_{xy}{}^1\delta_{x^2-y^2}{}^1$(55%) + $\pi^*_{yz}{}^1\pi_{xz}{}^1\delta_{x^2-y^2}{}^1$(24%) + $\pi^*_{yz}{}^1\delta^*_{xy}{}^1\pi_{xz}{}^1$(10%) | $^4TS_{\delta\text{-}Mn^{IV}=O}$ | HAT |
| | | | $^4TS_{\sigma\text{-}Mn^{IV}=O}$ | PCET |
| | | | $^4TS_{\delta'\text{-}Mn^{IV}=O}$ | PCET |
| $Fe^{III}$−O | $S = 5/2$ | $\delta^*_{xy}{}^1\pi^*_{yz}{}^1\pi^*_{xz}{}^1\delta^*_{x^2-y^2}{}^1\sigma^*_{z^2}{}^1$ (100%) | $^6TS_{Fe^{III}=O}$ | PT-ET |
| $Fe^{IV}$=O | $S = 2$ | $\delta^*_{xy}{}^1\pi^*_{xz}{}^1\pi_{yz}{}^0\delta^*_{x^2-y^2}{}^1\sigma^*_{z^2}{}^1$ (99%) | $^5TS_{Fe^{IV}=O}$ | HAT |
| $Fe^{V}$=O | $S = 3/2$ | $\pi^*_{yz}{}^1\delta^*_{xy}{}^1\delta^*_{x^2-y^2}{}^1$(43%) + $\pi^*_{yz}{}^1\delta^*_{xy}{}^1\pi_{xz}{}^1$ (25%) | $^4TS_{\pi\text{-}Fe^{V}=O}$ | HAT |
| | | | $^4TS_{\delta\text{-}Fe^{V}=O}$ | HAT |

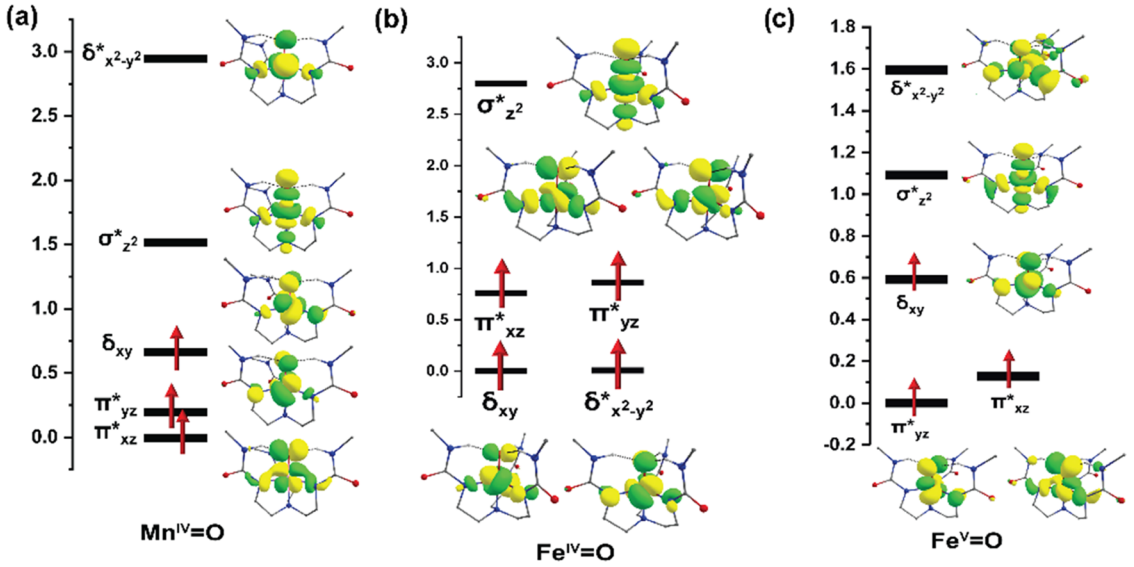


**Figure 1.** AILFT computed metal d-orbitals of (a) $[Mn^{IV}H_3buea(O)]^-$, (b) $[Fe^{IV}H_3buea(O)]^-$, and (c) $[Fe^{V}H_3buea(O)]$ species (energies are in eV). The isosurface value of 0.03 is employed to plot these orbitals.

species, we have performed DFT calculations, which reveal that all Mn/Fe−oxo(hydroxo) complexes in the series possess a high-spin ground state, which is in agreement with the available experimental results (Figures S1 and S2 and Tables 1 and S1a).[34,37,46,61−64] While the other intermediate/low-spin states of the various Mn species lying between 44.9 kJ/mol ($Mn^{IV}$−OH species, $S = 1$) and 201.5 kJ/mol (except the low-spin state of $Mn^{IV}$−OH species), the intermediate spin states of the Fe series are comparatively closely placed, lying within 71 kJ/mol for all species and much closer for $Fe^{III}$=O, $Fe^{III/IV}$−OH species. This indicates a greater possibility of two-state reactivity in the Fe series. The high-spin ground state for all (except Mn/$Fe^{IV}$=O species) and the trend in energy are captured in the CASSCF/NEVPT2-computed energetics (Figure S3).

The d-orbitals extracted from the *ab initio* ligand field theory (AILFT) approach using the CASSCF/NEVPT2 method reveals that the $[H_3buea]^{3-}$ ligand imposes a local trigonal geometry around the metal, generating a relatively weak ligand field, and all of the occupied orbitals are placed within a limit of ∼2 eV for both Mn and Fe species (Figures 1, S4, and S5). The AILFT computed orbital diagram is consistent with the orbital splitting expected for the trigonal bipyramidal geometry that yields a high-spin ground state for all cases studied (Figure S6). The $S = 3/2$ state as the ground state for $Fe^{V}$=O can also be correlated to the close-spaced AILFT orbitals. The H-bond cavity around the metal generates a relatively weaker ligand field with the $\pi^*_{yz}\pi^*_{xz}\delta_{xy}$ lying within 0.6 eV, resulting in the high-spin state. As the overall splitting is much higher, the mixing of the excited-state configuration with the ground state is unlikely to be favorable, and hence, these species are likely to show TSR/SSR-type reactivity.

In the present study, the state-average CASSCF calculations reveal a strong mixing of ground-state configuration with other electronic excited states, indicating a strong multiconfigurational character in $Mn^{III/IV}$=O, $Mn^{IV}$−OH, $Fe^{II/IV}$−OH, and $Fe^{V}$=O species (Table S1a). This kind of mixing was noticed in earlier studies.[65,66] For example, for the $Mn^{III}$=O species, CASSCF yields $\pi^*_{xz}{}^1\pi^*_{yz}{}^1\delta^*_{xy}{}^1\delta^*_{x^2-y^2}{}^1$ configuration have a weightage of 49% with another 48% contribution arising from the excitation of electrons from the $\pi^*_{yz} \rightarrow \sigma_{z^2}$ orbital, suggesting that both $\pi^*_{yz}$ and $\sigma_z{}^2$ orbitals are strongly mixed. Similar to the $Mn^{III}$=O species, a strong multideterminant character was found in the $Fe^{V}$=O species, where the significant contribution to the total wavefunction arises from the $\delta_{xy}{}^1\pi^*_{yz}{}^1\pi^*_{xz}{}^1$ (44%) configuration, which is found to be mixed with the $\delta_{xy}{}^1\pi^*_{yz}{}^1\sigma^*_{z^2}{}^1$ configuration (25%) (see the Supporting Information for other species details).

The Lewis acidity ($pK_a$) of the M−O/OH moiety decreases as $Mn^{III}$=O > $Fe^{III}$=O > $Fe^{II}$−OH > $Mn^{II}$−OH > $Mn^{IV}$=O > $Fe^{IV}$=O > $Mn^{III}$−OH > $Fe^{III}$−OH > $Mn^{V}$=O > $Mn^{V}$=O > $Fe^{IV}$−OH > $Mn^{IV}$−OH in the DMA medium, while the


https://doi.org/10.1021/acs.inorgchem.3c01632
Inorg. Chem. 2023, 62, 14931−14941

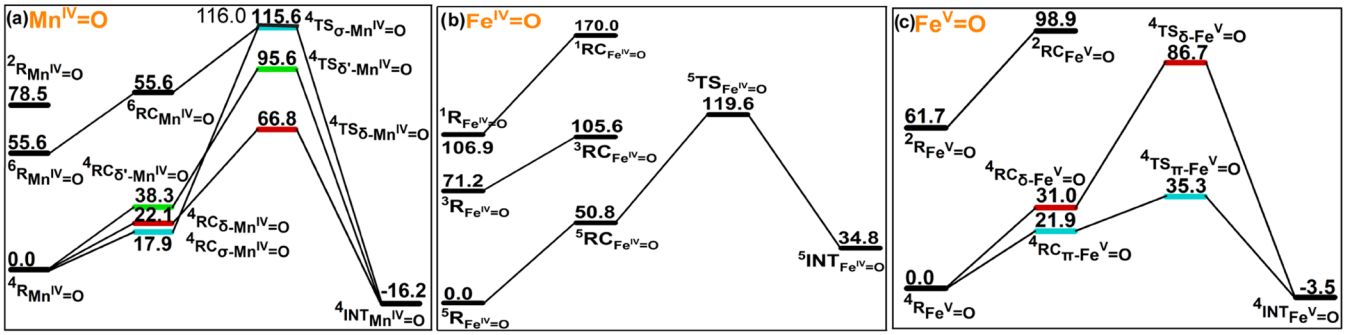


**Figure 2.** B3LYP-D3 computed energy profile diagram for the C−H bond activation of 9,10-dihydroanthracene (DHA) by (a) $[Mn^{IV}H_3buea(O)]^-$, (b) $[Fe^{IV}H_3buea(O)]^-$, and (c) $[Fe^{V}H_3buea(O)]$ catalysts (energies are in kJ/mol).

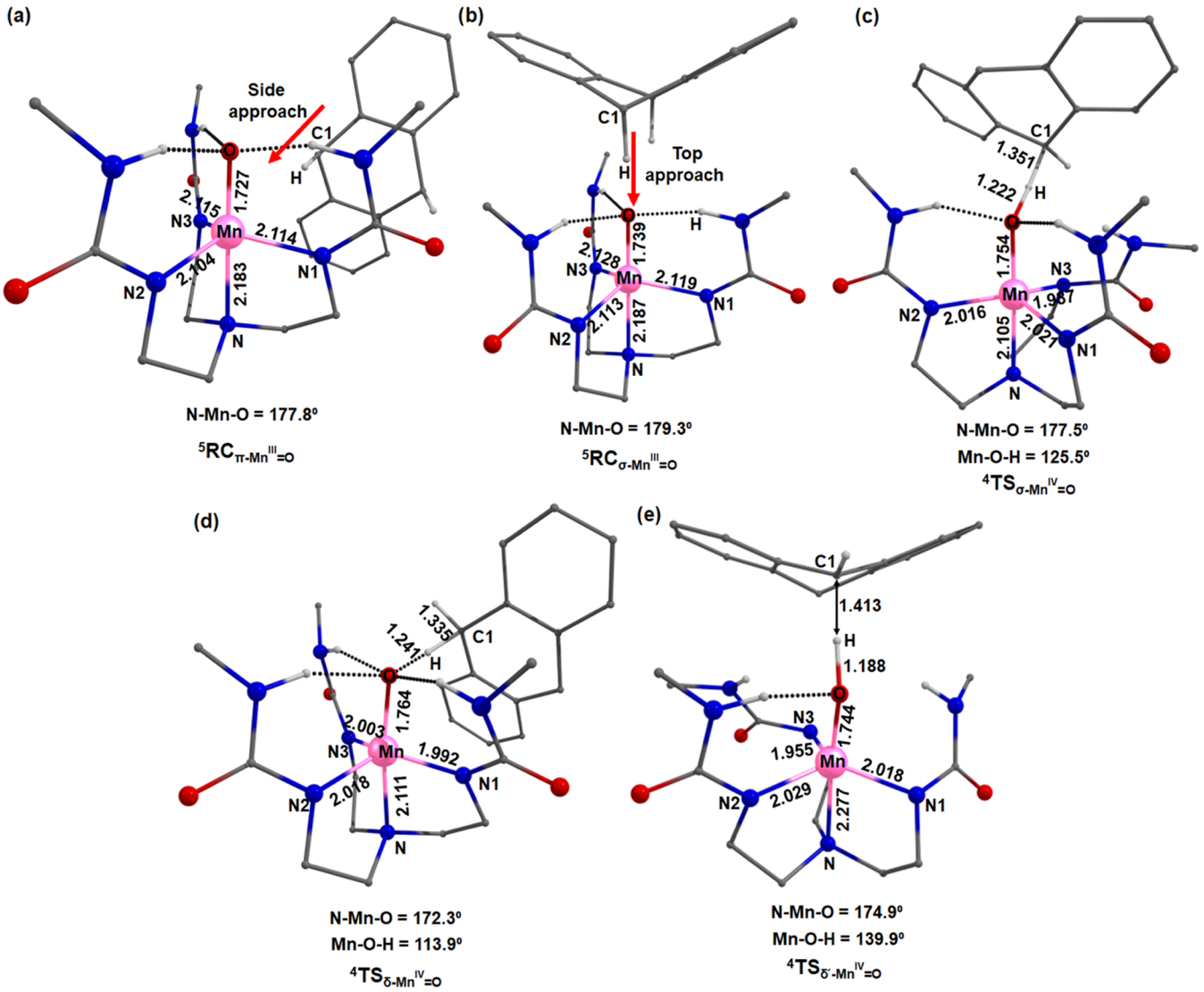


**Figure 3.** DFT-optimized geometries of (a−e) $^5RC_{\pi\text{-}Mn^{III}=O}$, $^5RC_{\sigma\text{-}Mn^{III}=O}$, $^4TS_{\sigma\text{-}Mn^{IV}=O}$, $^4TS_{\delta\text{-}Mn^{IV}=O}$, and $^4TS_{\delta'\text{-}Mn^{IV}=O}$, respectively.

calculated one-electron reduction potential values ($E_{1/2}$) of the corresponding half-reaction for each species follows the order $Fe^{IV}$−OH > $Fe^{V}$=O > $Mn^{IV}$−OH > $Mn^{V}$=O > $Fe^{IV}$−OH > $Mn^{IV}$=O > $Fe^{III}$−OH > $Mn^{III}$−OH > $Fe^{III}$=O > $Mn^{III}$=O > $Mn^{II}$−OH > $Fe^{II}$−OH against the $Fc^+$/Fc couple (Table S1b and Figure S7). We have also estimated the error bars in the redox potentials, as well as the p$K_a$ value, as suggested earlier,[67] and this is estimated to be 0.165 V and ±5, respectively.

*Reactivity of $Mn^{n+}$−X (n = II to V, X = O/OH) Species toward C−H Bond Activation.* Scheme S1 demonstrates the mechanism of the C−H activation step for the conversion of 9,10-dihydroanthracene (DHA) to anthracene using $M^{n+}$−oxo(OH) (where M = Mn/Fe, *n* = II to V) species as catalysts. In the Mn series, the intrinsic barrier for the C−H bond activation is the lowest (50.7 kJ/mol) for $Mn^{III}$=O species, followed by $Mn^{IV}$=O species (66.8 kJ/mol) (Figure 2). The


https://doi.org/10.1021/acs.inorgchem.3c01632
Inorg. Chem. 2023, 62, 14931−14941

energy barrier for other species is quite high, >80 kJ/mol, and therefore unreactive (Table S2).

For $[Mn^{III}H_3buea(O)]^{2-}$ species, we have found two reactant complexes, $^5RC_{\pi\text{-}Mn^{III}=O}$ (9.0 kJ/mol) and $^5RC_{\sigma\text{-}Mn^{III}=O}$ (26.6 kJ/mol), on the $S$ = 2 surfaces, with DHA found to approach either on a side-on fashion ($\pi$) or a head-on fashion ($\sigma$) (Figure 3a,b). CASSCF calculations reveal that for $^5RC_{\pi\text{-}Mn^{III}=O}$, the ground-state configuration of $\pi^*_{yz}{}^1\pi^*_{xz}{}^1\delta^*_{xy}{}^1\delta^*_{x^2-y^2}{}^1$ is contributing 42% to the total wavefunction, while the next highest contribution (28%) is originating from the $\pi^*_{xz} \rightarrow \sigma^*_{z^2}$ excitation. For $^5RC_{\sigma\text{-}Mn^{III}=O}$, the contribution from the ground-state configuration, $\pi^*_{yz}{}^1\delta^*_{xy}{}^1\ \pi^*_{xz}{}^1\ \delta^*_{x^2-y^2}{}^1$, is increased to 75%, indicating a lesser mixing to the ground-state configuration. The low-lying $^5RC_{\pi\text{-}Mn^{III}=O}$ state is connected to the lowest energy barrier of 50.7 kJ/mol ($^5TS_{\pi\text{-}Mn^{III}=O}$) for activating the C−H bond, while $^5TS_{\sigma\text{-}Mn^{III}=O}$ is lying at 12.2 kJ/mol uphill from $^5TS_{\pi\text{-}Mn^{III}=O}$ (Figures S8a,c). In $^5TS_{\pi\text{-}Mn^{III}=O}$ species, the total wavefunction is comprised of 59% contribution from the $\pi^*_{yz}{}^1\delta^*_{x^2-y^2}{}^1\delta^*_{xy}{}^1\pi^*_{xz}{}^1$ configuration with a significant mixing of a singly excited $\sigma^*_{z^2}{}^1\pi^*_{yz}{}^1\delta^*_{xy}{}^1\pi^*_{xz}{}^1$ configuration (30%). This mixing is found to be less in $^5TS_{\sigma\text{-}Mn^{III}=O}$, as expected (Table S3). In $^5TS_{\pi\text{-}Mn^{III}=O}$, the spin density on the metal remains unaltered ($\Delta\rho_{Mn}$ = 0.088) from $^5RC_{\pi\text{-}Mn^{III}=O}$ with no residual spin density ($\rho_{DHA}$ = 0.011) and a significant negative Mulliken charge ($e_{DHA}$ = −0.495) on the DHA moiety. This indicates that a proton is getting transferred from DHA to the catalyst-forming $MHA^-$ species during the transition state (Figure S8b).

We have performed the intrinsic bond orbital (IBO) representation of the wavefunction to qualitatively distinguish between various pathways followed by these species.[59,60] We begin our analysis by demonstrating the change in the $\alpha$ and $\beta$ spin IBOs of the C−H bond along the reaction coordinate. During the C−H bond activation via $^5TS_{\sigma\text{-}Mn^{III}=O}$ species, a proton and an electron travel together but follow two different pathways. In RC, both IBOs of $\alpha$ and $\beta$ spin of the C−H bond are found to be intact. As the reaction proceeds, at the transition state, while the proton is transferred to the oxo group, the electron is traveled to the metal center, leaving behind a radical ($\alpha$ or $\beta$) on the substrate, indicating a concerted PCET mechanism. On the other hand, in $^5TS_{\pi\text{-}Mn^{III}=O}$, the hydrogen is moved to the oxo group as a proton leaving behind both $\alpha$ and $\beta$ spin IBOs on the substrate and the corresponding electron is found to be delocalized to three carbon positions, indicating a PT-ET mechanism (Figure S9 and S10).

In $[Mn^{IV}H_3buea(O)]^-$ species, three different reactant complexes were optimized, namely, $^4RC_{\sigma\text{-}Mn^{IV}=O}$, $^4RC_{\delta\text{-}Mn^{IV}=O}$, and $^4RC_{\delta'\text{-}Mn^{IV}=O}$ (Figure S8d−f) with $^4RC_{\sigma\text{-}Mn^{IV}=O}$, being the lowest-lying among all RC and endothermic by 17.9 kJ/mol from the free catalyst. The lowest-lying $^4RC_{\sigma\text{-}Mn^{IV}=O}$ species possesses a $(\delta_{xy})^1(\pi_{xz}, \pi_{yz})^2$ configuration, which contributes 54% to the total wavefunction. This state is found to be mixed with the other singly excited states with contributions of 14 and 12%, arising from the transfer of $\alpha$-electron from $\pi_{yz}$ and $\pi_{xz}$ orbitals to $\sigma_{z^2}$ orbital, respectively. We have optimized another reactant complex species, $^4RC_{\delta'\text{-}Mn^{IV}=O}$, and similar to the lowest energy $^4RC_{\sigma\text{-}Mn^{IV}=O}$, the major contribution for this species is also originating from the $(\delta_{xy})^1(\pi_{xz}, \pi_{yz})^2$ configuration (56%). These two configurations differ in their second-highest contributing configuration to the wavefunction. For $^4RC_{\delta'\text{-}Mn^{IV}=O}$ species, the second contribution originates from the transfer of $\alpha$-electron from the $\delta_{xy}$ to $\delta_{x^2-y^2}$ orbital ($\pi_{xz}{}^1\pi_{yz}{}^1\delta_{x^2-y^2}{}^1$, 27%). In contrast, for $^4RC_{\delta\text{-}Mn^{IV}=O}$, several equal weightage excitations, such as $\delta_{xy}/\pi_{xz} \rightarrow \delta_{x^2-y^2}\ /\sigma^*_{z^2}$ (17%), $\pi_{xz} \rightarrow \sigma^*_{z^2}$ (17%), $\delta_{xy} \rightarrow \delta_{x^2-y^2}$ (15%), $\pi_{yz}/\pi_{xz} \rightarrow \delta_{x^2-y^2}/\sigma^*_{z^2}$ (15%), and $\delta_{xy} \rightarrow \sigma^*_{z^2}$ (12%), dominate the wavefunction. The reactant complex $^4RC_{\delta\text{-}Mn^{IV}=O}$ has the highest oxyl radical character (0.232) among all and is connected to the lowest energy barrier for the C−H activation, 66.8 kJ/mol associated with $^4TS_{\delta\text{-}Mn^{IV}=O}$ transition state. The energy barrier associated with $^4RC_{\sigma\text{-}Mn^{IV}=O}$ and $^4RC_{\delta'\text{-}Mn^{IV}=O}$ is 115.6 and 95.6 kJ/mol, respectively (Figure 2a). In $^4TS_{\delta\text{-}Mn^{IV}=O}$, the highest contribution (44%) to the total wavefunction comes from a doubly excited $\pi^*_{xz}{}^1\sigma^*_{z^2}{}^1\delta^*_{x^2-y^2}{}^1$ configuration originating from the $\delta^*_{xy}/\pi_{yz} \rightarrow \delta^*_{x^2-y^2}/\sigma^*_{z^2}$ electronic transition. This majorly contributing state is found to be heavily admixed with other doubly excited states arising from the $\pi_{yz}/\pi^*_{xz}$ to $\sigma^*_{z^2}/\delta^*_{x^2-y^2}$ (27%) and $\delta^*_{xy}/\pi^*_{xz}$ to $\sigma^*_{z^2}/\delta^*_{x^2-y^2}$ (11%) electron transfer. This mixing in the configurations is in line with the extended CASSCF [CAS (9,8)] calculations on the rate-determining $^4TS_{\delta\text{-}Mn^{IV}=O}$, where the highest contributing (29%) doubly excited state ($\sigma_z{}^1\delta^*_{x^2-y^2}{}^1\pi^*_{yz}{}^1\pi^*_{xz}{}^1\sigma^*_{z^2}{}^1$) is found to be mixed with another doubly and singly excited state $\delta^*_{x^2-y^2}{}^1\pi^*_{xz}{}^1\sigma^*_{z^2}{}^1$ (24%) and $\delta^*_{x^2-y^2}{}^1\pi^*_{yz}{}^1\pi^*_{xz}{}^1$ (19%), respectively (Figure 3c−e). From these calculations on all of the transition states, it is revealed that higher contributions from the excited-state configurations lower the energy barrier for the hydrogen atom transfer. For instance, the contribution of $(\delta_{xy})^1$ $(\pi_{xz}, \pi_{yz})^2$ is decreased in the order from $^4TS_{\sigma\text{-}Mn^{IV}=O}$ (38%) to $^4TS_{\delta'\text{-}Mn^{IV}=O}$ (27%) to $^4TS_{\delta\text{-}Mn^{IV}=O}$ (0%), and the barrier height also decreases in the same manner, even the ratio of decrease in barrier height matches the percentage of contribution (Figure 4) closely. Similar to the $Mn^{III}$=O species, these species are also following different mechanisms during the C−H bond activation process. If a C−H bond is cleaved following a HAT mechanism, the localized IBOs would be diminished from a C−H $\sigma$-bond and appear as a part of a newly forming O−H bond. As we move from RC to $^4TS_{\delta\text{-}Mn^{IV}=O}$, an IBO belonging to the $\alpha$-spin manifold is found to be transferred to the newly formed O−H $\sigma$-bond. The $\beta$ spin IBO remains intact on the C-atom of the substrate. In this pathway, the C−H bond is broken homolytically with the transfer of an electron along with the proton to the oxo group, leaving behind a radical on the substrate (Figure 5). However, the other two species follow the PCET mechanism (Figures S11 and S12). Our IBO analysis has shown that $Mn^{II}$−OH species reacts via the PT-ET mechanism, $Mn^{III/IV}$−OH species reacts via PCET, and $Mn^{V}$=O species reacts via the HAT mechanism (Figures S13−S16).

The above study suggests that if spin states of the same multiplicity lie within a small energy window (10−15 kJ/mol), there is a likely chance that both the states participate in the reactivity or the excited state becomes the ground state at the transition state due to the additional electronic flexibility that it enjoys. This reactivity, where the excited state of the same spin multiplicity is involved during the reaction, is called identical spin multistate reactivity (ISMR), as no spin inversion is required on this surface. Further, if the gap between these same multiplicity states is much larger (~80−100 kJ/mol), the excited states are unlikely to participate in the reactivity. It is important to also note here that when the states are coming very close to each other, their spin−orbit coupling is also expected to increase (see Table S1b) for computed spectral


https://doi.org/10.1021/acs.inorgchem.3c01632
Inorg. Chem. 2023, 62, 14931−14941

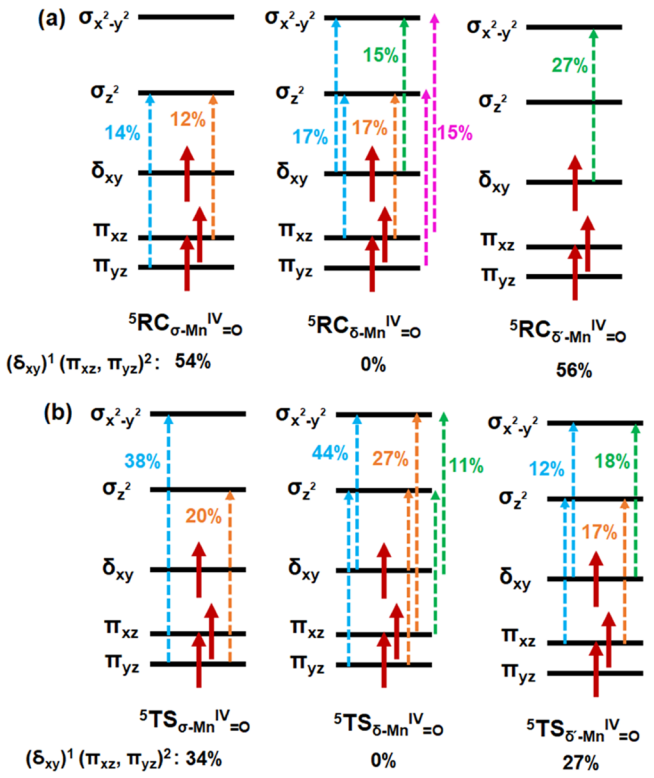


**Figure 4.** Electronic contributions in (a) reactant complexes and (b) transition states in $Mn^{IV}$=O.

parameters, including zero-field splitting, facilitating stronger mixing and greater reactivity (see below).

*Reactivity of $Fe^{n+}$–X (n = II to V, X = O/OH) Species toward C–H Bond Activation.* The barrier heights computed for the C–H bond activation of DHA by the Fe–O(OH) species reveal that only the $Fe^{III}$=O and $Fe^{V}$=O species possessing an energy barrier of <60 kJ/mol are reactive, while others are not (Figures S17–S19). The reactive $Fe^{III}$=O and $Fe^{V}$=O species react via PT–ET and HAT mechanisms, respectively (Figures S20–S22). The other unreactive $Fe^{II/III}$–OH reacts via PT–ET (Figures S23 and S24), $Fe^{IV}$–OH via PCET (Figure S25), and the $Fe^{IV}$=O species react via the HAT mechanism (Figure S26). This is indicative that the reactivity is not dependent on the reaction mechanism.

Similar to the previous Mn complexes, we found two reactant complexes for the $Fe^{V}$=O species, $^4RC_{\pi\text{-}Fe^{V}=O}$ and $^4RC_{\delta\text{-}Fe^{V}=O}$, varying the dominant electronic configuration contributing to the wavefunction (Figure 6). The $^4RC_{\pi\text{-}Fe^{V}=O}$ species is comprised of several equally weighted electronic states, i.e., $\delta_{xy}^{1}\pi_{yz}^{1}\delta_{x^2-y^2}^{1}$ (19%), $\sigma_{z^2}^{1}\pi_{yz}^{1}\delta_{x^2-y^2}^{1}$ (17%), $\delta_{xy}^{1}\pi_{xz}^{1}\delta_{x^2-y^2}^{1}$ (16%), $\delta_{xy}^{1}\sigma_{z^2}^{1}\delta_{x^2-y^2}^{1}$ (14%), $\pi_{xz}^{1}\sigma_{z^2}^{1}\delta_{x^2-y^2}^{1}$ (14%), and $\delta_{xy}^{1}\sigma_{z^2}^{1}\pi_{yz}^{1}$ (13%), while in $^4RC_{\delta\text{-}Fe^{V}=O}$, the significant contribution originates from the ground-state electronic configurations, $\pi_{xz}^{1}\delta_{xy}^{1}\pi_{yz}^{1}$ (42%) configuration, which is predominantly governed by the doubly and singly excited electronic states, is found to be the low-lying one (21.9 kJ/mol), with the other one at 9.1 kJ/mol higher in energy than $^4RC_{\pi\text{-}Fe^{V}=O}$. The highly admixed $^4RC_{\pi\text{-}Fe^{V}=O}$ species is connected to the lowest energy barrier, 35.3 kJ/mol ($^4TS_{\pi\text{-}Fe^{V}=O}$), and this transition state is exclusively dominated by doubly excited electronic states, $\pi_{xz}^{1}\sigma_{z^2}^{1}\delta_{x^2-y^2}^{1}$ and $\delta_{xy}^{1}\sigma_{z^2}^{1}\delta_{x^2-y^2}^{1}$, contributing 48 and 19% to the total wavefunction. The other one, $^4TS_{\delta\text{-}Fe^{V}=O,}$ is lying 51.4 kJ/mol higher in energy than $^4TS_{\pi\text{-}Fe^{V}=O}$. Both the $^4TS_{\pi\text{-}Fe^{V}=O}$ and $^4TS_{\delta\text{-}Fe^{V}=O}$ species follow a HAT mechanism.

Unlike the $Fe^{V}$=O species, the $Fe^{IV}$=O species ground-state electronic configuration is pure (100%: $\pi^{*}_{yz}{}^{1}\delta^{*}_{xy}{}^{1}\pi^{*}_{xz}{}^{1}\sigma^{*}_{z}{}^{2}{}^{1}$) and does not exhibit any of the mixing mentioned above and suggests that the absence of such mixing leads to very larger barrier heights (119.6 kJ/mol) and hence sluggish reactivity.

**Thermodynamics of the Mn/$Fe^{n+}$–O(OH) (*n* = II to V) Species toward Reactivity.** Further, we have analyzed the computed p$K_a$ values of the conjugate acid–base pairs and the redox potential $E_{1/2}$ values of the half-reactions involved in the C–H abstraction process. As we discussed already, the C–H activation by [$M^{n+}$=O/OH] species can occur in two ways: (i) a PT-ET mechanism and (ii) a PCET/HAT mechanism. In the PT-ET path, the species undergoes protonation forming [$M^{n+}$=OH/$OH_2$]$^+$ species and followed by an electron

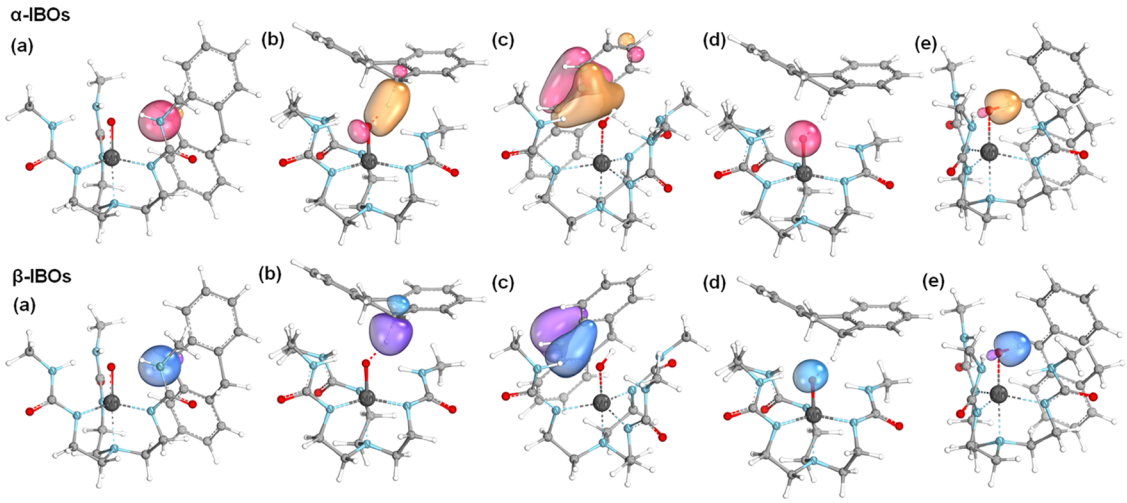


**Figure 5.** Changes in the C–H bond IBOs along the reaction coordinate for $Mn^{IV}$=O species in (a) reactant complex ($^5RC_{\delta\text{-}Mn^{IV}=O}$), (b) transition state ($^5TS_{\delta\text{-}Mn^{IV}=O}$) and (c) product ($^5INT_{Mn^{IV}=O}$) respectively. The O-cantered $\alpha$ and $\beta$ IBOs in the newly formed O–H bond are shown in (d) $^5TS_{\delta\text{-}Mn^{IV}=O}$ and (e) $^5INT_{Mn^{IV}=O,}$ respectively. Here, the pink and blue colors represent positive density, while orange and violet represent negative density.



https://doi.org/10.1021/acs.inorgchem.3c01632
Inorg. Chem. 2023, 62, 14931–14941

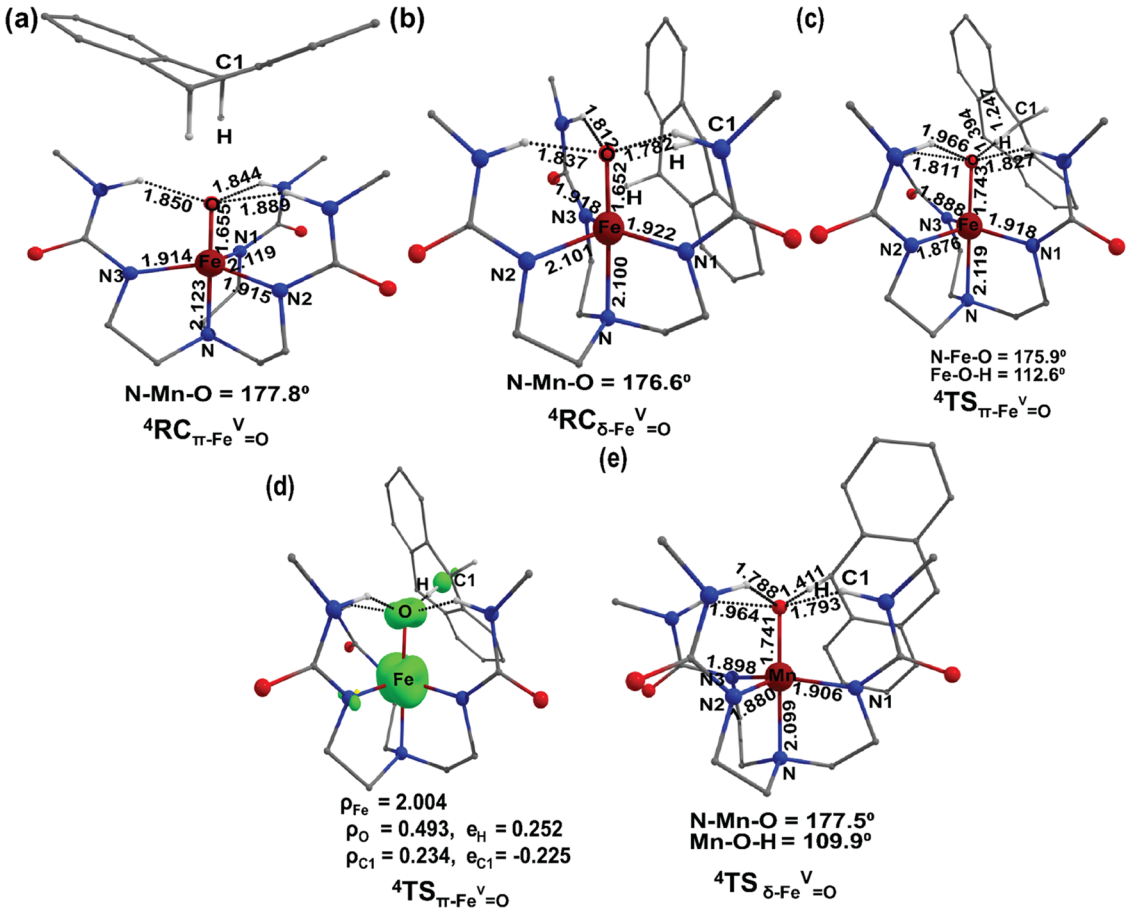


**Figure 6.** DFT-optimized structures (a–c) $^4RC_{\pi\text{-}Fe^V=O}$, $^4RC_{\delta\text{-}Fe^V=O}$, and $^4TS_{\pi\text{-}Fe^V=O}$. (d) Spin densities on Mn, oxo, and C1 (DHA) of $^4TS_{\pi\text{-}Fe^V=O}$ with the isosurface value of 0.03. Here, green (yellow) color denotes $\alpha(\beta)$-spin density and (e) DFT-optimized structure of $^4TS_{\delta\text{-}Fe^V=O}$ species.

transfer. The first step depends on the p$K_a$ value of the reactant, while the electron transfer step is dependent on the $E_{1/2}$ value of the half-reaction involved with the protonated species. In contrast to the PT-ET process, the PCET/HAT mechanism involves a concerted transfer of a proton as well as an electron, and this is governed either by the p$K_a$ or $E_{1/2}$ value of the reactants. Our computed data reveals that there are three different scenarios: (i) $Mn^{III}$=O and $Fe^{III}$=O species with higher p$K_a$ values of 24.4 and 19.4 can be expected to have proton transfer occur in the first step. (ii) Species that are strongly oxidizing, such as the $[Fe^{V/IV}H_3buea(O)]^{0/-1}$ couple, having a positive $E_{1/2}$ value of 0.15 eV vs $Fc^+$/Fc couple, offer a strong driving force for one-electron reduction, facilitating a concerted HAT mechanism. (iii) The species which are moderately basic (p$K_a$ < 12) and also have a less negative $E_{1/2}$ value compared to the PT-ET scenario, the reactivity was found to be controlled by both parameters. The $Mn^{IV}$=O species (p$K_a$ of 7.8 and $E_{1/2}$ value of −1.26 eV) follows this route. Thus, it ticks both the boxes in terms of reactivity and follows a concerted mechanism, however, with lesser reactivity. (iv) The unreactive nature of $Mn^{III/IV}$–OH, $Mn^V$=O, and $Fe^{IV}$=O is attributed to their low p$K_a$ values (<5) as well as highly negative one-electron redox potentials. Thus, these species do not tick on any of the boxes and hence are unreactive. Also, although the p$K_a$ values of $Mn^{II}$–OH and $Fe^{II}$–OH suggest the presence of a basic M–OH moiety, the basicity is not high enough for an efficient PT-ET mechanism. Therefore, the latter pairs are expected to show sluggish reactivity. In a similar way, $Fe^{III}$–OH being comparatively more acidic found to be unreactive. The probability of the other pathway, such as PCET/HAT for Mn/$Fe^{II}$–OH and $Fe^{III}$–OH species, can be eliminated here on the ground that their reduction potentials are highly negative ($E_{1/2}$ values for $Mn^{II}$–OH, $Fe^{II}$–OH, and $Fe^{III}$–OH are −9.1, −10.5, and −1.57 eV, respectively, against the $Fc^+$/Fc couple) for accepting an electron.[67] We have estimated the thermodynamic cycles for all of the species, and the reactivity pattern is in line with the computed p$K_a$ and $E_{1/2}$ values (Figure S27).

## DISCUSSION

The first hydrogen atom abstraction from DHA is known to be the rate-limiting step in metal–oxo chemistry,[68] and based on the computed barrier heights (Table S1a), it can be stated that the $Mn^{III}$=O, $Mn^{IV}$=O, $Fe^{III}$=O, and $Fe^V$=O species having an activation barrier of less than 70 kJ/mol are reactive while others are not. Even $Fe^{IV}$=O species, which is conventionally known to be extremely reactive, is unreactive in this ligand environment. These observations are consistent with available experimental data. Also, it is found that a high-oxidation state does not necessarily mean greater reactivity. While $Fe^V$=O is the most aggressive oxidant, $Mn^V$=O is sluggish or shows no reactivity. Similarly, the $Mn^{III}$=O species is more reactive than the $Mn^{IV}$=O species. This suggests that the oxidation state alone cannot decide the reactivity pattern.

We have demonstrated that the different reactivity pattern is attributed to the presence of multireference character in these


https://doi.org/10.1021/acs.inorgchem.3c01632
Inorg. Chem. 2023, 62, 14931–14941

species and on the availability of comparatively low-lying unoccupied orbital to accommodate electron transfer from the substrate during the C−H activation process. For $Mn^{III}$=O and $Fe^{III}$=O species, a proton is getting transferred during the transition state; therefore, the presence of a low-lying vacant orbital is not mandatory. For the $Mn^{II}$/$Fe^{III}$−OH species being a half-filled $d^5$ species, there are no d-electronic excited states, though crystal field splitting is smaller. For the $Mn^{IV}$−OH and $Fe^{IV}$−OH species, the respective highest lying $\delta^*_{x^2-y^2}$ and $\pi^*_{yz}$ orbitals are too high to accommodate the electron during the C−H activation process, making them unreactive. Similarly, although $Fe^{II}$−OH species show multiconfigurational character, one needs to keep in mind that metal−hydroxo species are generally less reactive than metal−oxo species. This is because the protonation of the oxo group diminishes the oxyl radical character substantially and reduces the electrophilicity of the oxo group. The presence of proton also enforces steric strain in the abstraction of C−H bonds leading to less reactivity. Thus, though the reactivity of $Fe^{II}$−OH is the highest among all hydroxide species studied due to the involvement of the excited state, it is significantly less reactive if we compare it with oxo species.

The rigid ligand framework of $[H_3Buea]^{3-}$ enforces trigonal bipyramidal geometry leading to a $2\pi$-$2\delta$-$1\sigma$ splitting pattern for the d-orbitals and results in a high-spin ground state for all of the species studied. Further, the oxo/hydroxo groups are involved in strong H-bonding interactions with the cavity imposed by the $[H_3Buea]^{3-}$ ligand. This results in a weaker ligand field than bare $Fe^{IV}$=O/OH species.[31] The overall CF splitting of the d-orbitals is found to be in the range of ∼1.0 to ∼3.5 eV, and this is nearly 2 times smaller than the other six-coordinate metal−oxo species.[69] The AILFT-computed orbitals suggest that the splitting increases with the oxidation state of metal ions for both Mn/Fe=O(OH) species with the exception of $Fe^{V}$=O species. Among Fe=O species, the $Fe^{V}$=O has the lowest gap of ∼1.6 eV, while the largest d-orbital CF splitting is found for $Fe^{IV}$=O species (∼2.75 eV). Among the Mn−OH complexes, the d-orbital CF splitting is very large for the $Mn^{III/IV}$−OH species (∼2.5−3.5 eV). Interestingly, this crystal field splitting is correlated to the reactivity, with $Mn^{III/IV}$−OH and $Fe^{IV}$=O species being unreactive and the $Fe^{V}$=O species showing the highest reactivity. Similarly, $Mn^{III}$=O has a gap of ∼2.25 eV, and $Mn^{IV}$=O has a slightly larger gap (∼3.0 eV); while both are reactive here, the former is more reactive compared to the latter. The experiments reported earlier support these observations.[68]

The conventional two-state reactivity concept is well established for both heme and nonheme $Fe^{IV}$=O species, wherein reactivity is often observed via the high-spin state.[26,70] Here, high spin is the default ground state, and hence, the necessity for a spin crossover to another state does not arise; therefore, one could expect a pure single-state reactivity (SSR) for all of these species. By performing *ab initio* CASSCF calculations on these species, we have found the following classifications: (i) pure SSR reactivities are observed in $S$ = 5/2 and $S$ = 2 surfaces with pure single-reference configuration for $Mn^{II}$−OH, $Fe^{III}$=O, and $Fe^{IV}$=O species, respectively. Also, SSR with OH, $Mn^{V}$=O, and $Fe^{IV}$−OH species, (ii) a conventional TSR is observed for $Fe^{III}$−OH species (Figure S2c). (iii) In addition to this, we have also detested a multistate reactivity, where states are strongly admixed with excited states of the same spin multiplicity in $Mn^{III}$=O, $Mn^{IV}$=O, $Fe^{II}$−OH, and $Fe^{V}$=O species. We analyzed the AILFT multireference configuration detected for $Mn^{III}$−OH and $Mn^{IV}$−OH species, which reveals that SSR with single-reference character observed for $Mn^{II}$−OH and $Fe^{III}$=O species is due to the absence of d-electronic excited states being a $d^5$ species, and in $Fe^{IV}$=O species, the $\sigma^*_{z^2}$ is strongly destabilized ($\Delta E$ ($\pi^*_{yz}$ − $\sigma_{z^2}$*) = ∼1.75 eV). Also, when the frontier d-orbital gap between the highest occupied and lowest unoccupied falls in the region of ∼1.0 to 1.5 eV (as in the case of $Mn^{III}$−OH, $Mn^{IV}$−OH, $Mn^{V}$=O, and $Fe^{IV}$−OH), strong mixing of the states is noticeable within the ground state. However, excited states are still far away, leading to an SSR-type reactivity for these species. When this gap is much lower (<1.0 eV), for example, in the case of $Mn^{IV}$=O, $Fe^{II}$−OH, and $Fe^{V}$=O, many close-lying states mix with each other, leading to higher reactivity called identical spin multistate reactivity (ISMR).

## CONCLUSIONS

A weak crystal field is found to bring several excited states of the same spin multiplicity closer to the ground state, resulting in a multireference character in $Mn^{III/IV}$=O, $Fe^{II}$−OH, and $Fe^{V}$=O species and dictates an identical spin multistate reactivity (ISMR) in various complexes. As the multireference character is absent in the $Fe^{IV}$=O species (and others), they lack electronic flexibility during the course of the reaction, leading to sluggish/no reactivity. Considering the well-established reactivity of various metal-oxo species through $\sigma$, $\pi$, and $\delta$ pathways sharing the same spin multiplicity, this observation strongly suggests the potential existence of ISMR-type reactivity beyond the examples presented.

To this end, we have studied a series of Fe/Mn−oxo(hydroxo) species using theoretical tools and proposed an intriguing role of the electronic excited states of the same spin multiplicity, which is found to rationalize the observed reactivity trend across various species that have different oxidation states or metal centers. As metalloenzymes' active sites have several H-bonding networks, a similar effect could be responsible for their superior catalytic abilities.

## ASSOCIATED CONTENT

### Supporting Information

The Supporting Information is available free of charge at https://pubs.acs.org/doi/10.1021/acs.inorgchem.3c01632.

Schematic representation of the C−H bond activation of 9,10-dihydroanthracene (DHA); comparative energy separation between the ground state and other excited states; crystal field splitting; changes of C−H bond IBO; ground state of all species with CASSCF-computed electronic configurations; important bonding parameters and spin densities, and a preprint of this manuscript is submitted to Chemarxiv, see reference 71 for details (PDF)

## AUTHOR INFORMATION

### Corresponding Author

**Gopalan Rajaraman** − *Department of Chemistry, Indian Institute of Technology Bombay, Mumbai 400076, India;* orcid.org/0000-0001-6133-3026; Email: rajaraman@chem.iitb.ac.in



https://doi.org/10.1021/acs.inorgchem.3c01632
*Inorg. Chem.* 2023, 62, 14931−14941

## Authors

**Asmita Sen** − *Department of Chemistry, Indian Institute of Technology Bombay, Mumbai 400076, India*

**Azaj Ansari** − *Department of Chemistry, Indian Institute of Technology Bombay, Mumbai 400076, India;* Present Address: Department of Chemistry, Central University of Haryana, Mahendragarh, Haryana 123301, India

**Abinash Swain** − *Department of Chemistry, Indian Institute of Technology Bombay, Mumbai 400076, India*

**Bhawana Pandey** − *Department of Chemistry, Indian Institute of Technology Bombay, Mumbai 400076, India*

Complete contact information is available at: https://pubs.acs.org/10.1021/acs.inorgchem.3c01632


## Notes

The authors declare no competing financial interest.

## ■ ACKNOWLEDGMENTS

The authors thank DST and SERB (CRG/2022/001697 and SB/SJF/2019-20/12) for funding. A.S./Ab.S. thanks CSIR/UGC for the fellowship and IITB for the computing facility.

## ■ REFERENCES


(1) Tolman, W. B. *Activation of Small Molecules: Organometallic and Bioinorganic Perspectives*; John Wiley & Sons, 2006.

(2) Vaillancourt, F. H.; Yin, J.; Walsh, C. T. SyrB2 in syringomycin E biosynthesis is a nonheme FeII α-ketoglutarate-and O2-dependent halogenase. *Proc. Natl. Acad. Sci. U.S.A.* **2005**, *102*, 10111−10116.

(3) Galonić, D. P.; Barr, E. W.; Walsh, C. T.; Bollinger, J. M.; Krebs, C. Two interconverting Fe (IV) intermediates in aliphatic chlorination by the halogenase CytC3. *Nat. Chem. Biol.* **2007**, *3*, 113−116.

(4) Yachandra, V. K.; Sauer, K.; Klein, M. P. Manganese cluster in photosynthesis: where plants oxidize water to dioxygen. *Chem. Rev.* **1996**, *96*, 2927−2950.

(5) Price, J. C.; Barr, E. W.; Tirupati, B.; Bollinger, J. M.; Krebs, C. The first direct characterization of a high-valent iron intermediate in the reaction of an α-ketoglutarate-dependent dioxygenase: a high-spin Fe (IV) complex in taurine/α-ketoglutarate dioxygenase (TauD) from *Escherichia coli*. *Biochemistry* **2003**, *42*, 7497−7508.

(6) Rohde, J.-U.; In, J.-H.; Lim, M. H.; Brennessel, W. W.; Bukowski, M. R.; Stubna, A.; Münck, E.; Nam, W.; Que, L. Crystallographic and spectroscopic characterization of a nonheme Fe (IV)= O complex. *Science* **2003**, *299*, 1037−1039.

(7) Rana, S.; Biswas, J. P.; Sen, A.; Clémancey, M.; Blondin, G.; Latour, J.-M.; Rajaraman, G.; Maiti, D. Selective C−H halogenation over hydroxylation by nonheme iron (IV)-oxo. *Chem. Sci.* **2018**, *9*, 7843−7858.

(8) McDonald, A. R.; Que, L., Jr. High-valent nonheme iron-oxo complexes: Synthesis, structure, and spectroscopy. *Coord. Chem. Rev.* **2013**, *257*, 414−428.

(9) Que, L., Jr.; Puri, M. The Amazing High-Valent Nonheme Iron-Oxo Landscape. *Bull. Jpn. Soc. Coord. Chem.* **2016**, *67*, 10−18.

(10) McDonald, A. R.; Que, L. Elusive iron (V) species identified. *Nat. Chem.* **2011**, *3*, 761−762.

(11) Pattanayak, S.; Jasniewski, A. J.; Rana, A.; Draksharapu, A.; Singh, K. K.; Weitz, A.; Hendrich, M.; Que, L., Jr.; Dey, A.; Sen Gupta, S. Spectroscopic and Reactivity Comparisons of a Pair of bTAML Complexes with FeV = O and FeIV = O Units. *Inorg. Chem.* **2017**, *56*, 6352−6361.

(12) Van Heuvelen, K. M.; Fiedler, A. T.; Shan, X.; De Hont, R. F.; Meier, K. K.; Bominaar, E. L.; Münck, E.; Que, L. One-electron oxidation of an oxoiron (IV) complex to form an [O═ FeV═ NR]+ center. *Proc. Natl. Acad. Sci. U.S.A.* **2012**, *109*, 11933−11938.

(13) Matson, E. M.; Park, Y. J.; Fout, A. R. Facile nitrite reduction in a nonheme iron system: Formation of an iron (III)-oxo. *J. Am. Chem. Soc.* **2014**, *136*, 17398−17401.

(14) MacBeth, C. E.; Golombek, A. P.; Young, V. G.; Yang, C.; Kuczera, K.; Hendrich, M. P.; Borovik, A. O2 activation by nonheme iron complexes: a monomeric Fe (III)-oxo complex derived from O2. *Science* **2000**, *289*, 938−941.

(15) Andris, E.; Navratil, R.; Jasik, J.; Puri, M.; Costas, M.; Que, L., Jr.; Roithová, J. Trapping iron (III)−oxo species at the boundary of the "Oxo Wall": insights into the nature of the Fe (III)−O bond. *J. Am. Chem. Soc.* **2018**, *140*, 14391−14400.

(16) Guo, M.; Corona, T.; Ray, K.; Nam, W. Heme and nonheme high-valent iron and manganese oxo cores in biological and abiological oxidation reactions. *ACS Cent. Sci.* **2019**, *5*, 13−28.

(17) Rice, D. B.; Massie, A. A.; Jackson, T. A. Manganese−Oxygen Intermediates in O−O Bond Activation and Hydrogen-Atom Transfer Reactions. *Acc. Chem. Res.* **2017**, *50*, 2706−2717.

(18) Massie, A. A.; Denler, M. C.; Cardoso, L. T.; Walker, A. N.; Hossain, M. K.; Day, V. W.; Nordlander, E.; Jackson, T. A. Equatorial Ligand Perturbations Influence the Reactivity of Manganese (IV)-Oxo Complexes. *Angew. Chem., Int. Ed.* **2017**, *56*, 4178−4182.

(19) Denler, M. C.; Massie, A. A.; Singh, R.; Stewart-Jones, E.; Sinha, A.; Day, V. W.; Nordlander, E.; Jackson, T. A. Mn IV-Oxo complex of a bis (benzimidazolyl)-containing N5 ligand reveals different reactivity trends for Mn IV-oxo than Fe IV-oxo species. *Dalton Trans.* **2019**, *48*, 5007−5021.

(20) Li, X.-X.; Guo, M.; Qiu, B.; Cho, K.-B.; Sun, W.; Nam, W. High-Spin Mn (V)-Oxo Intermediate in Nonheme Manganese Complex-Catalyzed Alkane Hydroxylation Reaction: Experimental and Theoretical Approach. *Inorg. Chem.* **2019**, *58*, 14842−14852.

(21) Biswas, S.; Mitra, A.; Banerjee, S.; Singh, R.; Das, A.; Paine, T. K.; Bandyopadhyay, P.; Paul, S.; Biswas, A. N. A High Spin Mn (IV)-Oxo Complex Generated via Stepwise Proton and Electron Transfer from Mn (III)−Hydroxo Precursor: Characterization and C−H Bond Cleavage Reactivity. *Inorg. Chem.* **2019**, *58*, 9713−9722.

(22) Lee, Y.-M.; Kim, S.; Ohkubo, K.; Kim, K.-H.; Nam, W.; Fukuzumi, S. Unified Mechanism of Oxygen Atom Transfer and Hydrogen Atom Transfer Reactions with a Triflic Acid-Bound Nonheme Manganese (IV)−Oxo Complex via Outer-Sphere Electron Transfer. *J. Am. Chem. Soc.* **2019**, *141*, 2614−2622.

(23) Halbach, R. L.; Gygi, D.; Bloch, E. D.; Anderson, B. L.; Nocera, D. G. Structurally characterized terminal manganese (IV) oxo tris (alkoxide) complex. *Chem. Sci.* **2018**, *9*, 4524−4528.

(24) Yoon, H.; Morimoto, Y.; Lee, Y.-M.; Nam, W.; Fukuzumi, S. Electron-transfer properties of a nonheme manganese (iv)−oxo complex acting as a stronger one-electron oxidant than the iron (iv)−oxo analogue. *Chem Commun.* **2012**, *48*, 11187−11189.

(25) Wu, X.; Seo, M. S.; Davis, K. M.; Lee, Y.-M.; Chen, J.; Cho, K.-B.; Pushkar, Y. N.; Nam, W. A highly reactive mononuclear nonheme manganese (IV)−Oxo complex that can activate the strong C−H bonds of alkanes. *J. Am. Chem. Soc.* **2011**, *133*, 20088−20091.

(26) Schröder, D.; Shaik, S.; Schwarz, H. Two-state reactivity as a new concept in organometallic chemistry. *Acc. Chem. Res.* **2000**, *33*, 139−145.

(27) Kumar, D.; Hirao, H.; Que, L.; Shaik, S. Theoretical Investigation of C− H Hydroxylation by (N4Py) FeIV O2+: An Oxidant More Powerful than P450? *J. Am. Chem. Soc.* **2005**, *127*, 8026−8027.

(28) Hirao, H.; Kumar, D.; Que, L., Jr.; Shaik, S. Two-state reactivity in alkane hydroxylation by nonheme iron− oxo complexes. *J. Am. Chem. Soc.* **2006**, *128*, 8590−8606.

(29) Huang, J.; Li, C.; Wang, B.; Sharon, D. A.; Wu, W.; Shaik, S. Selective chlorination of substrates by the halogenase SyrB2 is controlled by the protein according to a combined quantum mechanics/molecular mechanics and molecular dynamics study. *ACS Catal.* **2016**, *6*, 2694−2704.

(30) Borowski, T.; Noack, H.; Radon, M.; Zych, K.; Siegbahn, P. E. Mechanism of selective halogenation by SyrB2: a computational study. *J. Am. Chem. Soc.* **2010**, *132*, 12887−12898.

(31) Shaik, S.; Hirao, H.; Kumar, D. Reactivity of high-valent iron−oxo species in enzymes and synthetic reagents: a tale of many states. *Acc. Chem. Res* **2007**, *40*, 532−542.
(32) Shaik, S.; Chen, H.; Janardanan, D. Exchange-enhanced reactivity in bond activation by metal−oxo enzymes and synthetic reagents. *Nat. Chem.* **2011**, *3*, 19−27.
(33) Cho, K.-B.; Shaik, S.; Nam, W. Theoretical investigations into C−H Bond activation reaction by nonheme MnIVO complexes: multistate reactivity with no oxygen rebound. *J. Phys. Chem. Lett.* **2012**, *3*, 2851−2856.
(34) Parsell, T. H.; Behan, R. K.; Green, M. T.; Hendrich, M. P.; Borovik, A. Preparation and Properties of a Monomeric MnIV− Oxo Complex. *J. Am. Chem. Soc.* **2006**, *128*, 8728−8729.
(35) Shirin, Z.; Hammes, B. S.; Young, V. G.; Borovik, A. Hydrogen Bonding in Metal Oxo Complexes: Synthesis and Structure of a Monomeric Manganese (III)− Oxo Complex and Its Hydroxo Analogue. *J. Am. Chem. Soc.* **2000**, *122*, 1836−1837.
(36) Taguchi, T.; Gupta, R.; Lassalle-Kaiser, B.; Boyce, D. W.; Yachandra, V. K.; Tolman, W. B.; Yano, J.; Hendrich, M. P.; Borovik, A. Preparation and properties of a monomeric high-spin MnV−oxo complex. *J. Am. Chem. Soc.* **2012**, *134*, 1996−1999.
(37) Gupta, R.; Borovik, A. Monomeric MnIII/II and FeIII/II complexes with terminal hydroxo and oxo ligands: probing reactivity via O− H bond dissociation energies. *J. Am. Chem. Soc.* **2003**, *125*, 13234−13242.
(38) Hill, E. A.; Weitz, A. C.; Onderko, E.; Romero-Rivera, A.; Guo, Y.; Swart, M.; Bominaar, E. L.; Green, M. T.; Hendrich, M. P.; Lacy, D. C.; Borovik, A. S. Reactivity of an FeIV-oxo complex with protons and oxidants. *J. Am. Chem. Soc.* **2016**, *138*, 13143−13146.
(39) Frisch, M.; Trucks, G.; Schlegel, H.; Scuseria, G.; Robb, M.; Cheeseman, J.; Scalmani, G.; Barone, V.; Petersson, G.; Nakatsuji, H. *Gaussian 09*, revision D. 01; Gaussian Inc, 2009.
(40) Becke, A. D. Density-functional thermochemistry. V. Systematic optimization of exchange-correlation functionals. *J. Chem. Phys.* **1997**, *107*, 8554−8560.
(41) Sen, A.; Vyas, N.; Pandey, B.; Rajaraman, G. Deciphering the mechanism of oxygen atom transfer by nonheme Mn IV−oxo species: an ab initio and DFT exploration. *Dalton Trans.* **2020**, *49*, 10380−10393.
(42) Ansari, A.; Kaushik, A.; Rajaraman, G. Mechanistic Insights on the ortho-Hydroxylation of Aromatic Compounds by Nonheme Iron Complex: A Computational Case Study on the Comparative Oxidative Ability of FerriC−Hydroperoxo and High-Valent FeIV = O and FeV = O Intermediates. *J. Am. Chem. Soc.* **2013**, *135*, 4235−4249.
(43) Zhurko, G.; Zhurko, D. ChemCraft, version 1.6, 2009. http://www.chemcraftprog.com.
(44) Weigend, F.; Ahlrichs, R. Balanced basis sets of split valence, triple zeta valence and quadruple zeta valence quality for H to Rn: Design and assessment of accuracy. *Phys. Chem. Chem. Phys.* **2005**, *7*, 3297−3305.
(45) Marenich, A. V.; Cramer, C. J.; Truhlar, D. G. Universal solvation model based on solute electron density and on a continuum model of the solvent defined by the bulk dielectric constant and atomic surface tensions. *J. Phys. Chem. B* **2009**, *113*, 6378−6396.
(46) Gupta, R.; MacBeth, C. E.; Young, V. G.; Borovik, A. Isolation of monomeric MnIII/II− OH and MnIII− O complexes from water: evaluation of O− H bond dissociation energies. *J. Am. Chem. Soc.* **2002**, *124*, 1136−1137.
(47) Shook, R. L.; Peterson, S. M.; Greaves, J.; Moore, C.; Rheingold, A. L.; Borovik, A. Catalytic reduction of dioxygen to water with a monomeric manganese complex at room temperature. *J. Am. Chem. Soc.* **2011**, *133*, 5810−5817.
(48) Yamanaka, S.; Kawakami, T.; Nagao, H.; Yamaguchi, K. Effective exchange integrals for open-shell species by density functional methods. *Chem. Phys. Lett.* **1994**, *231*, 25−33.
(49) Cramer, C. J. *Essentials of Computational Chemistry: Theories and Models*; John Wiley & Sons, 2013.
(50) Angeli, C.; Bories, B.; Cavallini, A.; Cimiraglia, R. Third-order multireference perturbation theory: The n-electron valence state perturbation-theory approach. *J. Chem. Phys.* **2006**, *124*, No. 054108.
(51) Angeli, C.; Cimiraglia, R.; Evangelisti, S.; Leininger, T.; Malrieu, J.-P. Introduction of n-electron valence states for multi-reference perturbation theory. *J. Chem. Phys.* **2001**, *114*, 10252−10264.
(52) Olsen, J. The CASSCF method: A perspective and commentary. *Int. J. Quantum Chem.* **2011**, *111*, 3267−3272.
(53) Angeli, C.; Cimiraglia, R.; Malrieu, J.-P. N-electron valence state perturbation theory: a fast implementation of the strongly contracted variant. *Chem. Phys. Lett.* **2001**, *350*, 297−305.
(54) van Leest, N. P.; de Bruin, B. Revisiting the Electronic Structure of Cobalt Porphyrin Nitrene and Carbene Radicals with NEVPT2-CASSCF Calculations: Doublet versus Quartet Ground States. *Inorg. Chem.* **2021**, *60*, 8380−8387.
(55) van Leest, N. P.; Tepaske, M. A.; Oudsen, J.-P. H.; Venderbosch, B.; Rietdijk, N. R.; Siegler, M. A.; Tromp, M.; van der Vlugt, J. I.; de Bruin, B. Ligand redox noninnocence in [CoIII (TAML)] 0/−complexes affects nitrene formation. *J. Am. Chem. Soc.* **2019**, *142*, 552−563.
(56) Neese, F. The ORCA program system. *WIREs Comput. Mol. Sci.* **2012**, *2*, 73−78.
(57) Neese, F. Software update: the ORCA program system, version 4.0. *WIREs Comput. Mol. Sci.* **2017**, *8*, 73−78.
(58) van Lenthe, E.; Baerends, E.-J.; Snijders, J. G. Relativistic regular two-component Hamiltonians. *J. Chem. Phys.* **1993**, *99*, 4597−4610.
(59) Klein, J. E.; Knizia, G. cPCET versus HAT: A Direct Theoretical Method for Distinguishing X−H Bond-Activation Mechanisms. *Angew. Chem., Int. Ed.* **2018**, *57*, 11913−11917.
(60) Knizia, G. Intrinsic atomic orbitals: An unbiased bridge between quantum theory and chemical concepts. *J. Chem. Theory Comput.* **2013**, *9*, 4834−4843.
(61) Shirin, Z.; Borovik, A.; Young, V. G., Jr. Synthesis and structure of a Mn III (OH) complex generated from dioxygen. *Chem. Commun.* **1997**, *20*, 1967−1968.
(62) Taguchi, T.; Stone, K. L.; Gupta, R.; Kaiser-Lassalle, B.; Yano, J.; Hendrich, M. P.; Borovik, A. Preparation and properties of an Mn IV−hydroxide complex: proton and electron transfer at a mononuclear manganese site and its relationship to the oxygen evolving complex within photosystem II. *Chem. Sci.* **2014**, *5*, 3064−3071.
(63) Dey, A.; Hocking, R. K.; Larsen, P.; Borovik, A. S.; Hodgson, K. O.; Hedman, B.; Solomon, E. I. X-ray Absorption Spectroscopy and Density Functional Theory Studies of [(H3buea) FeIII-X] n-(X= S2-, O2-, OH-): Comparison of Bonding and Hydrogen Bonding in Oxo and Sulfido Complexes. *J. Am. Chem. Soc.* **2006**, *128*, 9825−9833.
(64) Lacy, D. C.; Gupta, R.; Stone, K. L.; Greaves, J.; Ziller, J. W.; Hendrich, M. P.; Borovik, A. Formation, Structure, and EPR Detection of a High Spin FeIV−Oxo Species Derived from Either an FeIII−Oxo or FeIII−OH Complex. *J. Am. Chem. Soc.* **2010**, *132*, 12188−12190.
(65) Sen, A.; Rajaraman, G. Can you break the oxo-wall? A multiconfigurational perspective. *Faraday Discuss.* **2022**, *234*, 175−194.
(66) Sen, A.; Ansari, M.; Rajaraman, G. Mechanism of Hydroboration of CO2 Using an Fe Catalyst: What Controls the Reactivity and Product Selectivity? *Inorg. Chem.* **2023**, *62*, 3727−3737.
(67) Bím, D.; Alonso-Gil, S.; Srnec, M. From Synthetic to Biological Fe4S4 Complexes: Redox Properties Correlated to Function of Radical S-Adenosylmethionine Enzymes. *ChemPlusChem* **2020**, *85*, 2534−2541.
(68) Parsell, T. H.; Yang, M.-Y.; Borovik, A. C−H Bond Cleavage with Reductants: Re-Investigating the Reactivity of Monomeric MnIII/IV−Oxo Complexes and the Role of Oxo Ligand Basicity. *J. Am. Chem. Soc.* **2009**, *131*, 2762−2763.
(69) Leto, D. F.; Massie, A. A.; Rice, D. B.; Jackson, T. A. Spectroscopic and computational investigations of a mononuclear


https://doi.org/10.1021/acs.inorgchem.3c01632
*Inorg. Chem.* 2023, 62, 14931−14941

manganese (IV)-oxo complex reveal electronic structure contributions to reactivity. *J. Am. Chem. Soc.* **2016**, *138*, 15413−15424.
(70) Shaik, S. Two-State Reactivity: Personal Recounting of its Conception and Future Prospects. *Isr. J. Chem.* **2020**, *60*, 938−956.
(71) Rajaraman, G.; Sen, A.; Swain, A.; Pandey, B.; Ansari, A. Identical Spin Multistate Reactivity Towards C−H Bond Activation in High-valent Fe/Mn-Oxo/Hydroxo Species *ChemRxiv* 2022, DOI: 10.26434/chemrxiv-2022-2sqgf.



https://doi.org/10.1021/acs.inorgchem.3c01632
*Inorg. Chem.* 2023, 62, 14931−14941